Direct numerical simulation of a turbulent wind over a wavy water surface

O. A. Druzhinin,[1] Y. I. Troitskaya,[1,2] and S. S. Zilitinkevich[2,3]

[1] Parameterization of the wind-water-waves interaction is a key problem of the air-sea system modeling. Of most importance are water waves with sufficiently large steepness, when nonlinear effects related to the boundary layer separation and vortex generation in the wind flow are well pronounced. Known experimental techniques (contact methods and particle image velocimetry) are not yet able to provide a full, detailed understanding of the wind flow in the viscous sublayer and the buffer region. As an alternative, we consider direct numerical simulations (DNS). In the present paper we discuss numerical algorithm and results of DNS of a turbulent wind flow over a wavy water surface. Waves with maximum steepness of $ka = 0.2$, wave age $0 < c/u* < 10$, and Reynolds number $Re = 15,000$ are considered. Full, 3-D Navier-Stokes equations are solved in curvilinear coordinates in a reference frame moving with the wave phase speed c. DNS results show that an instantaneous velocity field is characterized by the presence of well-pronounced separation zones in the vicinity of the wave crests whereas the average velocity field is nonseparating. We also perform a comparison of the DNS results with the predictions of a theoretical quasi-linear model of the wind-wave interaction.

1. Introduction

[2] The processes of momentum, heat and moisture transfer at the air-sea interface are of primary importance for climate formation mechanisms on both regional and global scales. In the present weather prediction models these exchange processes are characterized by bulk coefficients which are formulated on the basis of the parameterization of known experimental field and laboratory data. The bulk coefficients are strongly dependent on the details of the wind-waves interaction which at present are still not well understood [*Fairall et al.*, 2003]. The most complicated problem of the experimental research is related to the measurements of the wind flow properties in a thin layer in the vicinity of the water surface combining the viscous sublayer and the adjacent buffer region of the boundary layer and especially in wave troughs. The typical width of this layer is on the order of 1 mm and usually much smaller than the surface wave amplitude. Contact measurement techniques, including those using wave-following probes, do not allow obtaining detailed properties of the wind flow in this layer [*Donelan et al.*, 2005; *Hsu et al.*, 1981; *Hsu and Hsu*, 1983]. Methods based on the particle image velocimetry (PIV)

technique [*Adrian*, 1991] are capable of measuring 2-D instant wind velocity fields at the distance on the order of 1 mm from the water surface [*Reul et al.*, 1999; *Veron et al.*, 2007; *Troitskaya et al.*, 2010, 2011], sufficient for studying the flow in the upper viscous sublayer and the buffer region in the case of sufficiently weak winds with dynamical velocity less than 10 cm/s. Although obtaining 3-D fields in the airflow above waves is an unresolved experimental problem.

[3] The numerical experiment can be regarded as an advanced alternative to the laboratory and field measurements. In particular, in advantage to the most sophisticated experimental PIV technique, direct numerical simulations (DNS) provides statistical ensembles of instant 3-D vector velocity fields suitable for further statistical analysis. Attempts to model numerically the interaction of a turbulent wind flow with surface water waves were commenced practically since the creation of first supercomputers. Early numerical models were based on the ensemble- (Reynolds-) averaged, stationary, two-dimensional Navier-Stokes (or RANS) equations [*Gent and Taylor*, 1976; *Chalikov*, 1986; *Al-Zanaidi and Hui*, 1984].

[4] These equations employ a closure procedure relating the unknown turbulent (Reynolds) stresses to the gradient of the mean fields via a turbulent viscosity function. Whereas this semiempirical modeling is attractive due to its simplicity and has provided useful results concerning the behavior of the mean velocity, pressure and fluctuations of the wind flow over water waves, it also has a number of disadvantages. Perhaps, the most essential disadvantage of RANS models is its inability to predict the properties of the wind flow in the vicinity of the water surface, in the viscous sublayer and in

[1]Geophysical Research, Institute of Applied Physics, Russian Academy of Sciences, Nizhni Novgorod, Russia.
[2]Department of Radiophysics, Lobachevsky State University of Nizhni Novgorod, Nizhni Novgorod, Russia.
[3]Division of Atmospheric Sciences, Department of Physical Sciences, Finnish Meteorological Institute, Helsinki, Finland.
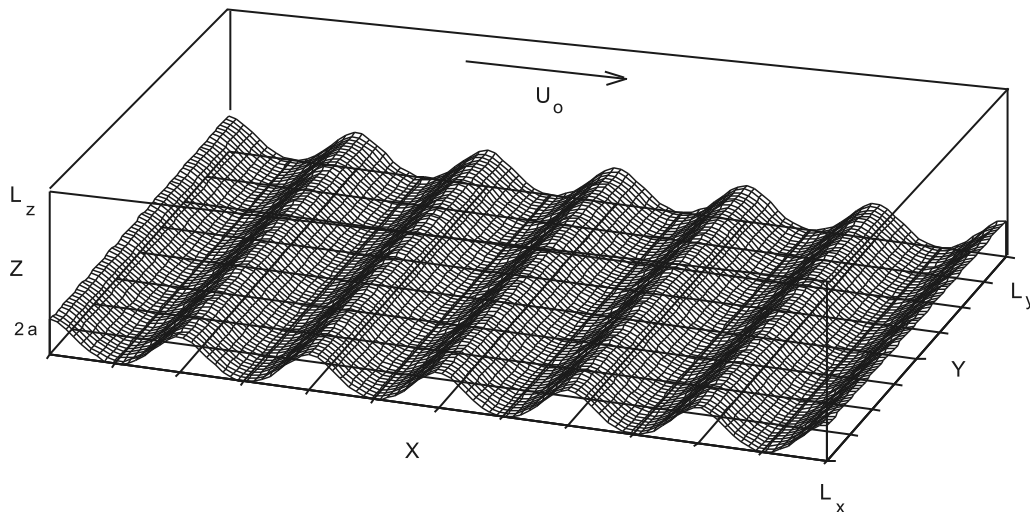
Figure 1. Schematic of the flow.

the buffer region. In this regard, RANS models are actually on par with the experimental methods.

[5] More complicated, large eddy simulation models were developed later [cf. *Sullivan et al.*, 2008]. These models consider three-dimensional and nonstationary Navier-Stokes equations and are capable of resolving the large-scale vortex structure of the wind flow. However, they still do not provide the description of the flow properties in the intermediate vicinity of the water surface since the first grid node in the vertical direction typically is located in the logarithmic region of the boundary layer.

[6] At present, perhaps the only method which can resolve the above problem is based on DNS. In their pioneering study *Sullivan et al.* [2000] first employed DNS to study the turbulent wind flow over surface waves for Reynolds number (based on the bulk wind flow velocity, surface wavelength λ, and air molecular viscosity) $Re = 8800$ and wave steepness $ka = 0.1$ (where k is the wave number and a is the wave amplitude). Later *Yang and Shen* [2010] employed DNS to study the turbulent wind flow over waves with maximum steepness $ka = 0.25$ and $Re \approx 10,000$. DNS provides full description of the wind flow properties on all physically significant scales, up to the molecular dissipation scale. However, the disadvantage of this approach is its inability to prescribe a sufficiently large Reynolds number (on the order of 10^5 and more) typical for the wind-wave interaction observed in the laboratory studies.

[7] In the present paper, we perform direct numerical simulation of a turbulent wind flow over water wavy surface for Reynolds number $Re = 15,000$ and maximum wave steepness $ka = 0.2$. Therefore, Re in our DNS is almost twice as large as compared to the one prescribed by *Sullivan et al.* [2000] ($Re = 8800$) and 50% larger than the Reynolds number prescribed by *Yang and Shen* [2010] ($Re = 9943$) whereas the maximum wave steepness is close to the value 0.25 prescribed by *Yang and Shen* [2010].

2. Governing Equations and Numerical Method

[8] We perform direct numerical simulation of a turbulent Couette flow over a wavy water surface. The schematic of

the numerical experiment is presented in Figure 1. A Cartesian framework is considered where x axis is oriented along the mean wind flow, z axis is directed vertically upward, and y axis is transversal to the mean flow and parallel to the wavefront. A two-dimensional water wave is considered with amplitude a, wavelength λ and phase velocity c, and periodical in the x direction. In the present study a maximum wave steepness is $ka = 2\pi a/\lambda = 0.2$. DNS is performed in a reference frame moving with the wave phase velocity, so that the horizontal coordinate in the moving framework is $x = x' - ct$, where x' is the coordinate in the laboratory reference frame. Therefore, in the moving reference frame, the lower boundary representing the wave surface is stationary. A no-slip boundary condition is considered at the lower boundary, so that the wind flow velocity at this boundary coincides with the orbital velocities of particles in the water wave and is independent of time. The computational domain with sizes $L_x = 6\lambda$, $L_y = 4\lambda$ and $L_z = \lambda$ in the x, y, and z directions is considered, and the wind flow is assumed to be periodical in the x and y directions. Also a no-slip boundary condition is prescribed at the upper horizontal plane which is assumed to be moving with bulk velocity U_0 in the x direction. This condition provides external momentum source due to the action of the viscous shear stress which compensates the viscous dissipation in the boundary layer and makes the flow statistically stationary.

[9] Numerical algorithm is based on the integration of full, 3-D Navier-Stokes equations for an incompressible fluid. In the dimensionless variables, the governing equations are written in the form

$$\frac{\partial U_i}{\partial t} + \frac{\partial (U_i U_j)}{\partial x_j} = -\frac{\partial P}{\partial x_i} + \frac{1}{Re}\frac{\partial^2 U_i}{\partial x_j \partial x_j}, \qquad (1)$$

$$\frac{\partial U_j}{\partial x_j} = 0, \qquad (2)$$

where $U_i(i = 1, 2, 3) = (U, V, W)$ are wind flow velocity components in the Cartesian framework $x_i(i = 1, 2, 3) = (x, y, z)$ and P is the dimensionless pressure. In (1) and (2)

the coordinates and velocities are normalized by the wavelength λ and bulk velocity U_0, and the pressure is normalized by ρU_0^2 (where ρ is the air density). The Reynolds number equals to $Re = \frac{U_0 \lambda}{\nu}$, where ν is the air molecular viscosity.

[10] In order to avoid the strong geometrical nonlinearity during integration of (1) and (2) related to the lower wavy boundary (Figure 1), a conformal mapping is employed which transforms the plane (x, z) in the Cartesian frame to a plane (ξ, η) in curvilinear coordinates as

$$x = \xi - a \exp(-k\eta) \sin k\xi \qquad (3)$$

$$z = \eta + a \exp(-k\eta) \cos k\xi. \qquad (4)$$

[11] This mapping transforms the lower wavy boundary $z_b(x) = a \cos k\xi(x)$ into a plane boundary at $\eta = 0$. It easy to show that for small, finite wave amplitude a the shape of the boundary $z_b(x)$, up to the terms of order $O(k^2 a^3)$, coincides with the Stokes wave asymptotic solution [Gent and Taylor, 1976]

$$z_b(x) = a \cos kx + \frac{1}{2} a^2 k (\cos 2kx - 1). \qquad (5)$$

[12] In addition we employ a mapping over the vertical coordinate η in the form

$$\eta = 0.5 \left(1 + \frac{\tanh \tilde{\eta}}{\tanh 1.5} \right), \qquad (6)$$

where $-1.5 < \tilde{\eta} < 1.5$. Mapping (6) introduces a nonuniform spacing of the computational nodes in the vertical direction, with stretching in the middle of the domain (for $\tilde{\eta} \approx 0$ which corresponds to $z \approx \eta \approx 0.5$) and clustering near boundaries (for $\tilde{\eta} \approx \pm 1.5$ and $z \approx \eta \approx 0$ and 1).

[13] Due to the conformal properties of the mapping (3) and (4), the following relationships hold:

$$\frac{\partial \xi}{\partial x} = \frac{1}{J} \frac{\partial x}{\partial \xi} = \frac{1}{J} \frac{\partial z}{\partial \eta}, \qquad (7)$$

$$\frac{\partial \xi}{\partial z} = \frac{1}{J} \frac{\partial z}{\partial \xi} = -\frac{1}{J} \frac{\partial x}{\partial \eta}, \qquad (8)$$

where $J = \left(\frac{\partial x}{\partial \xi} \right)^2 + \left(\frac{\partial x}{\partial \eta} \right)^2$ is the Jacobian of the mapping (3) and (4). Due to (7) and (8) the derivatives over coordinates x and z in (1) and (2) are replaced by the derivatives over ξ and η according to

$$\frac{\partial}{\partial x} = \frac{\partial \xi}{\partial x} \frac{\partial}{\partial \xi} - \frac{\partial \xi}{\partial z} \frac{\partial}{\partial \eta}, \frac{\partial}{\partial z} = \frac{\partial \xi}{\partial x} \frac{\partial}{\partial \eta} + \frac{\partial \xi}{\partial z} \frac{\partial}{\partial \xi} \qquad (9)$$

and the Laplasian operator in curvilinear coordinates (ξ, η) is rewritten as

$$\frac{\partial^2}{\partial x_j \partial x_j} = \frac{1}{J} \left(\frac{\partial^2}{\partial \xi^2} + \frac{\partial^2}{\partial \eta^2} \right) + \frac{\partial^2}{\partial y^2}. \qquad (10)$$

[14] According to (6) the derivative over stretched coordinate $\tilde{\eta}$ is related to the derivative over η as

$$\frac{\partial}{\partial \eta} = 2 \tanh 1.5 \cosh \tilde{\eta} \frac{\partial}{\partial \tilde{\eta}}. \qquad (11)$$

[15] Equations (1) and (2) are discretized in a rectangular domain with sizes $0 < \xi < 6$, $0 < y < 4$, and $-1.5 < \tilde{\eta} < 1.5$ by employing a finite difference method of the second-order accuracy on a uniform staggered grid consisting of $360 \times 240 \times 180$ nodes. Thus the grid spacing in the horizontal and transversal direction equals $\Delta x = \Delta y = 1/60$ and corresponds approximately to 7.5 viscous wall units $z_* = 1/(Re u_*)$ (where u^* is dynamical wind velocity). The grid spacing in the vertical direction near boundary approximately equals $\Delta z = 0.33 z^*$ and according to (6) increases monotonically to $\Delta z \approx 8 z^*$ at z = 0.5.

[16] The integration of (1,2) is advanced in time using the second-order accuracy Adams-Bashforth method in two stages at each time step n [Belotserkovski, 1984; Fletcher, 1988]. First, for the evaluation of the velocity value at a new, $n+1$, time step an intermediate velocity $\tilde{U}_i$ is computed using the velocity values obtained at the preceding time steps, U_i^{n-1} and U_i^n, as

$$\tilde{U}_i = U_i^n + \left(\frac{3}{2} F_i(U_i^n) - \frac{1}{2} F_i(U_i^{n-1}) \right) \Delta t, \qquad (12)$$

where flux $F_i(U_i)$ is evaluated as

$$F_i(U_i) = -\frac{\partial (U_i U_j)}{\partial x_j} + \frac{1}{Re} \frac{\partial^2 U_i}{\partial x_j \partial x_j}. \qquad (13)$$

[17] Further the pressure field at the $n+1$ time step is computed by solving the Poisson equation in the form

$$\frac{\partial^2 P^{n+1}}{\partial x_j \partial x_j} = \frac{1}{\Delta t} \frac{\partial \tilde{U}_j}{\partial x_j}. \qquad (14)$$

[18] Equation (14) is solved by an iteration procedure in curvilinear coordinates in the form

$$\left(\frac{\partial^2}{\partial \xi^2} + \frac{\partial^2}{\partial y^2} + \frac{\partial^2}{\partial \eta^2} \right) P_k^{n+1} = \frac{1}{J} \frac{\partial \tilde{U}_i}{\partial x_j} + \left(1 - \frac{1}{J} \right) \frac{\partial^2 P_{k-1}^{n+1}}{\partial y^2}, \qquad (15)$$

where k is the iteration number. Equation (15) is solved by employing FFT over ξ, y coordinates and Gauss elimination method over the η coordinate. The iteration procedure is stopped if the condition max $|P_k - P_{k-1}|$/max $|P_{k-1}| < 0.01$ is satisfied. Ordinarily, this condition is reached after 3–5 iterations. The new velocity at $n+1$ time step satisfying the incompressibility condition (2) is then computed as

$$U_i^{n+1} = \tilde{U}_i - \frac{\partial P^{n+1}}{\partial x_j} \Delta t. \qquad (16)$$

[19] At the lower plane boundary ($\eta = 0$) the no-slip (Dirichlet) condition is prescribed. Thus, the flow velocity

here coincides with the orbital velocities of the particles in the surface water wave

$$U_b^0(\xi, y) = c(ka\cos kx(\xi, \eta) - 1), \tag{17}$$

$$V_b^0(\xi, y) = 0, \tag{18}$$

$$W_b^0(\xi, y) = cka\sin\ kx(\xi, \eta). \tag{19}$$

[20] At the upper boundary at $\eta = 1$ a no-slip condition is prescribed with respect to the plane moving with nondimensional velocity $1 - c$ in the form

$$U_b^1 = 1 - c, \tag{20}$$

$$V_b^0(\xi, y) = 0, \tag{21}$$

$$W_b^0(\xi, y) = 0. \tag{22}$$

[21] Periodical boundary conditions are prescribed at the side boundaries of the computational domain, at $x = 0, 6$ and $y = 0, 4$.

[22] The flow is initialized as a weakly perturbed Couette flow in the form $U_i = z\delta_{ix} + u_{if}$ where $i = x, y, z$, and u_{if} is the fluctuation field with small (about 0.05) amplitude. The integration is performed with time step $\Delta t = 1/600$. Equations (1) and (2) are integrated until time moment $t = 100$ when all transients die off and a statistically stationary flow regime sets. (One dimensionless time unit equals approximately 20 viscous wall time units $1/(u_*^2 Re)$.) Further, the integration is performed until time $t = 200$. During the time interval $100 \leq t \leq 200$ the mean flow and fluctuation fields are evaluated. The averaging is performed over the spanwise y coordinate, time, and the wave spatial period $\lambda = 1$ in the streamwise x direction. The instantaneous fields for averaging are sampled at time moments $t_k, k = 1, \ldots, 500$ with time step $\Delta_{av}t = 0.2$. The averaging over the wavelength is performed as a window averaging.

[23] Therefore, for a given field $f(x, y, z, t)$ a phase-averaged field, $<f>(x, z)$, is evaluated as

$$\langle f \rangle(x, z) = \frac{1}{6N_t N_y} \sum_{j=1}^{N_y} \sum_{k=1}^{N_t} \sum_{n=0}^{5} f(x + n\lambda, y_j, z, t_k) \tag{23}$$

and the dispersion is evaluated as

$$\langle f^2 \rangle(x, z) = \frac{1}{6N_t N_y} \sum_{j=1}^{N_y} \sum_{k=1}^{N_t} \sum_{n=0}^{5} f^2(x + n\lambda, y_j, z, t_k), \tag{24}$$

where $N_y = 240$, $N_t = 500$ and $0 < x < 1$. The fluctuation is further obtained in the form

$$f'(x, z) = \left(\langle f^2 \rangle(x, z) - \langle f \rangle^2(x, z)\right)^{1/2}. \tag{25}$$

[24] In the case of an impulse flux $<U_x U_z>$ in the sum (24) the product $U_x U_z$ is substituted instead of f^2, and in (25) the difference ($<U_x U_z> - <U_x><U_z>$) is considered.

[25] A mean vertical profile of the field f, $[f](z)$, is obtained by an additional averaging of the phase-average $<f>(x, z)$ along the streamwise coordinate as

$$[f](z) = \frac{1}{N_x} \sum_{i=1}^{N_x/6} \langle f \rangle(x_i, z). \tag{26}$$

[26] The difference between the phase-average field $<f>$ (x, z) and the mean profile $[f]$ (z) gives the wave-induced mean field, $f_w(x, z) = <f>(x, z) - [f](z)$.

3. Validation of the Numerical Algorithm

[27] In order to validate the numerical algorithm presented above in section 2 we performed three test runs. In the first test run (case a) a plane lower boundary was considered and the Reynolds number was prescribed to be equal $Re = 15,000$. In the second and third test runs (case b) we considered the flow parameters close to the parameters in DNS of *Sullivan et al.* [2000]: the phase velocity $c = 0.25$ and the wave steepness $ka = 0.2$ and $ka = 0.1$, and the Reynolds number $Re = 10,000$.

3.1. Plane Lower Boundary, $Re = 15,000$

[28] The results obtained in this case are presented in Figures 2a and 2b. Figures 2a and 2b show the vertical mean profile of the horizontal velocity component $u^+(z^+)$ where the normalized velocity and vertical coordinate are $u^+ = <U_x>/u_*$ and $z^+ = z/z_*$. The numerical profile is compared with asymptotic solutions for the viscous sublayer

$$u^+ = z^+ \tag{27}$$

and the logarithmic region

$$u^+ = A\ln z^+ + B, \tag{28}$$

where $A = 2.44$ and $B = 5.7$. The dynamical velocity is evaluated from the turbulent momentum flux, $\tau = -[U_x'' U_z'']$, as

$$u_* = \tau^{1/2} \tag{29}$$

for sufficiently large z (i.e., in the region sufficiently far away from the boundary, where τ is constant). The viscous length scale is defined by

$$z_* = \frac{1}{u_* Re}. \tag{30}$$

[29] In the considered run these parameters are found to be equal to $u_* = 0.0263$ and $z_* = 0.00253$. The coefficients A and B in the asymptotic solution (28) are evaluated by a best fit procedure and in general agreement with well known results [*Monin and Yaglom*, 1971; *Sullivan et al.*, 2000].

[30] Figure 2b shows the vertical profiles of the fluctuations of the velocity components $u' \equiv U_x'$, $v' \equiv U_y'$ and $w' \equiv U_z'$, normalized by the dynamical velocity u_*, and compares our numerical results with the experimental data of *Aydin and Leutheusser* [1991] and DNS results of *Papavassiliou and Hanratty* [1997], obtained for somewhat
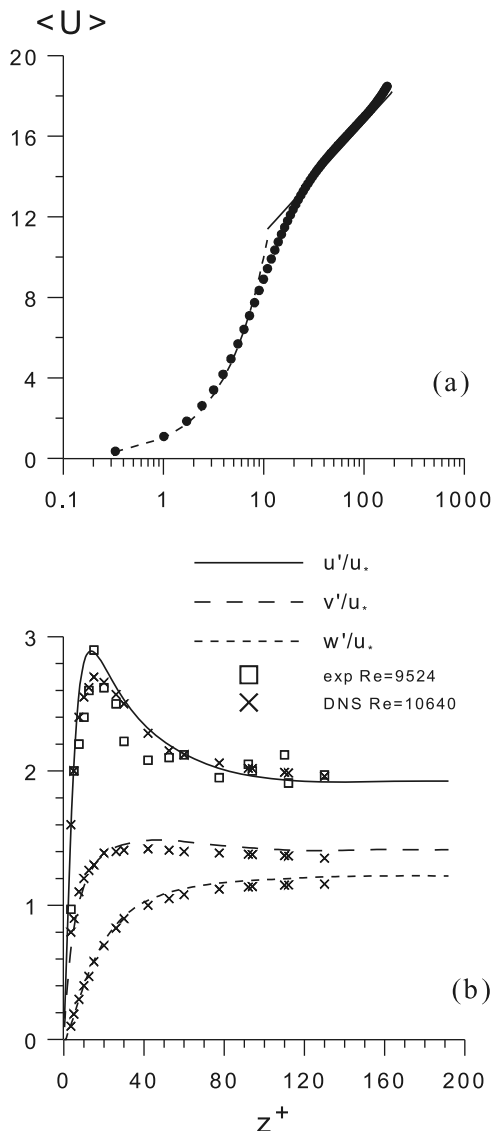
Figure 2. Profiles of the (a) mean horizontal velocity and (b) velocity fluctuations obtained in DNS with plane lower boundary.

lower Reynolds numbers. The figure shows a good agreement between our DNS results and known experimental and numerical results. Note also that the results in Figure 2 are in good agreement with the DNS results obtained by *Sullivan et al.* [2000] in their test runs (not shown here).

3.2. Wave Steepness $ka = 0.2$ and $ka = 0.1$, Phase Velocity $c = 0.25$, $Re = 10,000$

[31] Figures 3a–3d compare our DNS results with the results of DNS by *Sullivan et al.* [2000], obtained in this case (although, the Reynolds number of 8800 prescribed by Sullivan et al. was somewhat lower).

[32] Figures 3a and 3c compare vertical mean profiles of the horizontal velocity normalized by the dynamical velocity u_*, roughness length z_0 and coefficient A in the logarithmic asymptotic law (28). In the case $ka = 0.2$ these parameters are $u_* = 0.0325$, $z_0 = 0.0043$ and $A = 2.86$; in the case $ka = 0.1$, the dynamical velocity and roughness are $u_* = 0.031$, $z_0 = $ 0.0023 and the same coefficient A. The corresponding values of the dynamical velocity and roughness length obtained by *Sullivan et al.* [2000] are $u^* = 0.0342$, $z_0 = 0.0054$ for $ka = 0.2$ and $u^* = 0.0319$, $z_0 = 0.0028$ for $ka = 0.1$ and the coefficient $A = 2.94$ in both cases. Figures 3b and 3d compare the profiles of the velocity fluctuations and turbulent impulse flux taking into account the contribution of the wave-induced fields, u_w, v_w, w_w и τ_w. In both cases of $ka = 0.2$ and $ka = 0.1$ the agreement between our DNS results and the results of *Sullivan et al.* [2000] can be regarded as satisfactory.

[33] Therefore, the results of the test runs validate the numerical algorithm developed in section 2 for DNS of the turbulent wind flow over a wavy water surface.

4. Numerical Results

[34] DNS was performed for the wave steepness in the interval $0 \leq ka \leq 0.2$ and phase velocity $0 \leq c \leq 0.3$ for Reynolds number $Re = 15,000$. The corresponding wave age parameter, c/u_* was in the interval $0 \leq c/u_* \leq 10$.

[35] Figures 4 and 5 show the instantaneous vorticity modulus obtained in DNS for wave steepness $ka = 0.2$ and phase velocity $c = 0.05$ (wave age $c/u_* \approx 1.7$) (Figure 4) and $c = 0.2$ ($c/u_* \approx 7$) (Figure 5). Figures 6 and 7 show the distributions of the phase-average x and z velocity components (Figures 6a, 6b, 7a, and 7b), pressure (Figures 6c and 7c), and turbulent momentum flux (Figures 6d and 7d).

[36] The vorticity modulus (or a square root of the enstrophy) is evaluated as

$$\omega = \left(\omega_j \omega_j\right)^{1/2} \tag{31}$$

were the vorticity jth component is

$$\omega_j = \varepsilon_{jkl} \frac{\partial U_k}{\partial x_l}. \tag{32}$$

[37] Figure 4 presents the distribution of ω in plane (x, z) at $y = 0$ (Figures 4a and 4d), plane (x, y) at $z = 0.042$ (Figures 4b and 4e), and plane (y, z) at $x = 4.25$ (Figures 4c and 4f) obtained for $c = 0.05$. Figure 5 shows the distribution of ω in the same (x, z) and (x, y) planes (Figures 5a and 5b) and in (y, z) plane at $x = 3$ (Figure 5c). Figure 4b (for $c = 0.05$, $c/u_* \approx 1.7$) shows that the vorticity is mostly concentrated in thread-like vortex structures. These vortices have a horseshoe shape and resemble well-known λ vortices extensively studied in the case of a "classical" boundary layer over a solid plane boundary [*Moin and Kim*, 1985]. In the considered case these vortices are initiated in the viscous sublayer in the vicinity of wave crests and further separate and enter the logarithmic region of the flow. In the case $c = 0.2$ ($c/u_* \approx 7$, cf. Figure 5) these λ vortices are still present but far less distinguished in the vicinity of the wavy boundary as compared to the case $c/u_* \approx 1.7$.

[38] The distribution of the vorticity field above the wavy boundary was extensively studied by *Yang and Shen* [2010]. Their DNS results also show that in the case of slow waves with $c/u_* = 2$ the vorticity is concentrated mostly in horseshoe-like vortices separating from the wave surface, whereas for faster waves (with $c/u_* = 14$) these are
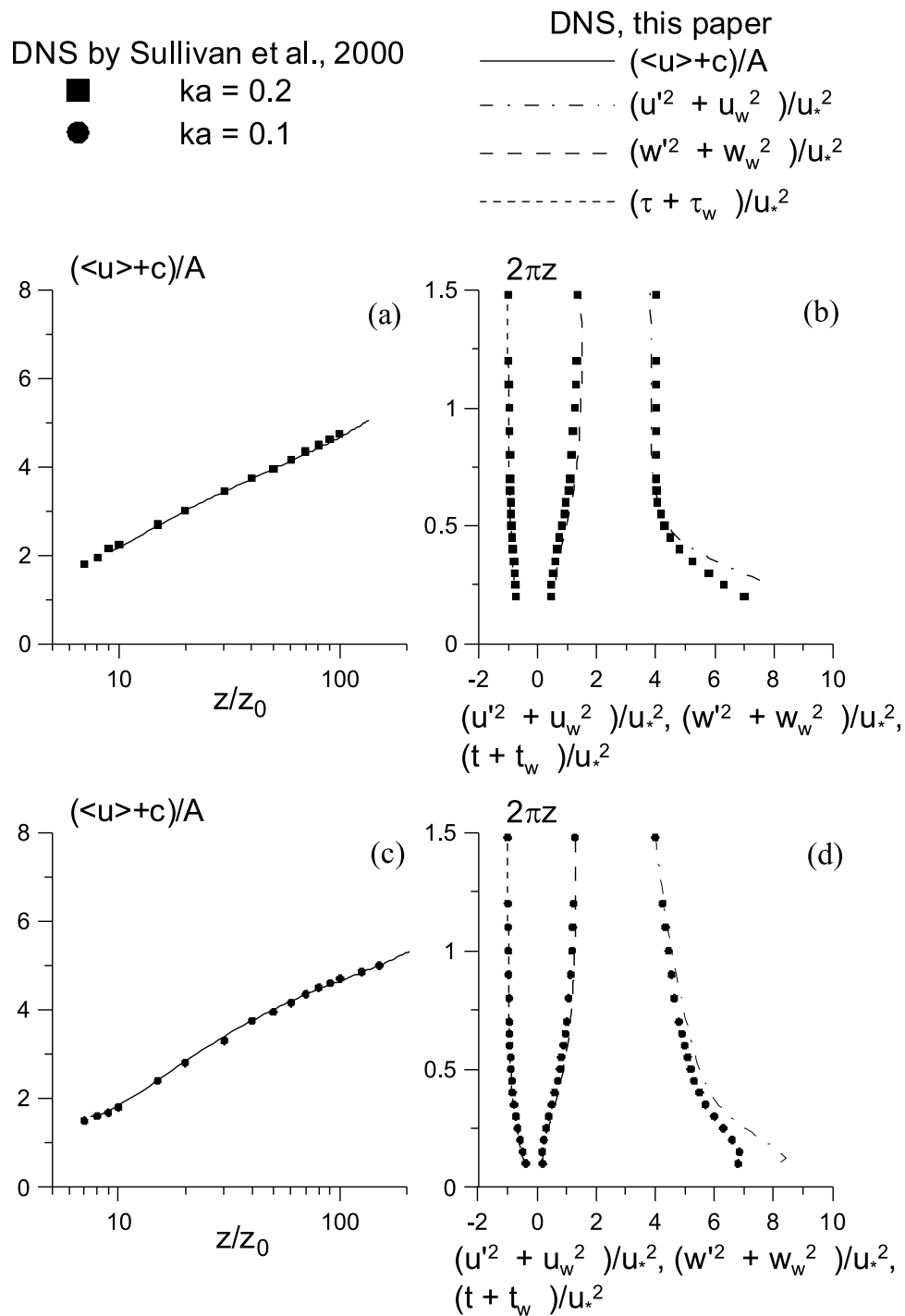
Figure 3. Profiles of the (a, c) mean horizontal velocity and (b, d) velocity fluctuations and turbulent momentum flux obtained in DNS for wavy lower boundary with $ka = 0.2$ (Figures 3a and 3b) and $ka = 0.1$ (Figures 3c and 3d) and $Re = 10{,}000$. Roughness length $z_0 = 0.0043$ (Figure 3a) and $z_0 = 0.0028$ (Figure 3c). Symbols are DNS by *Sullivan et al.* [2000], curves are this DNS.
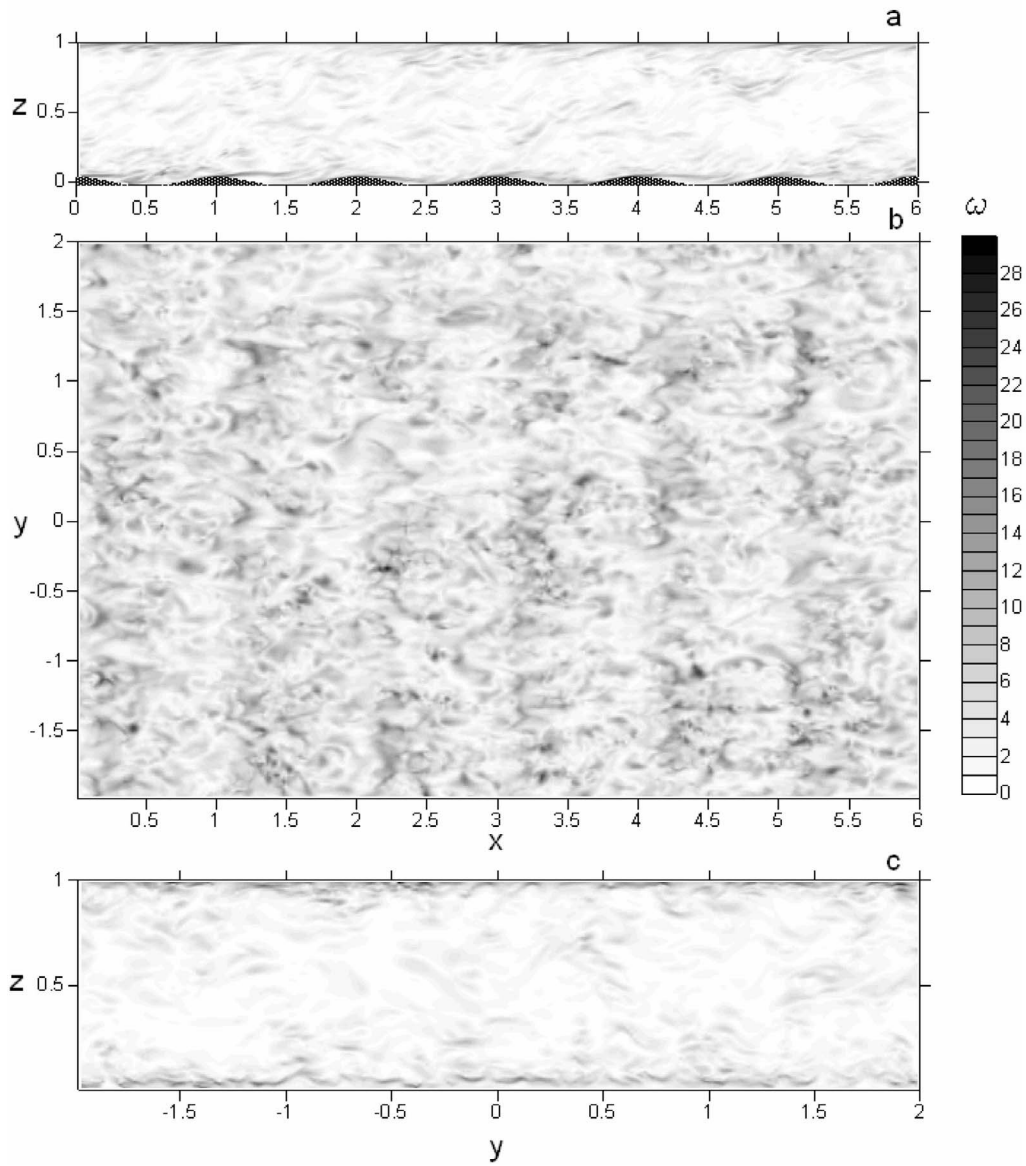
Figure 4. Instantaneous field of the vorticity modulus obtained in DNS with $ka = 0.2$ and $c = 0.05$ in the (a) (x, z) plane at $y = 0$, (b) (x, y) plane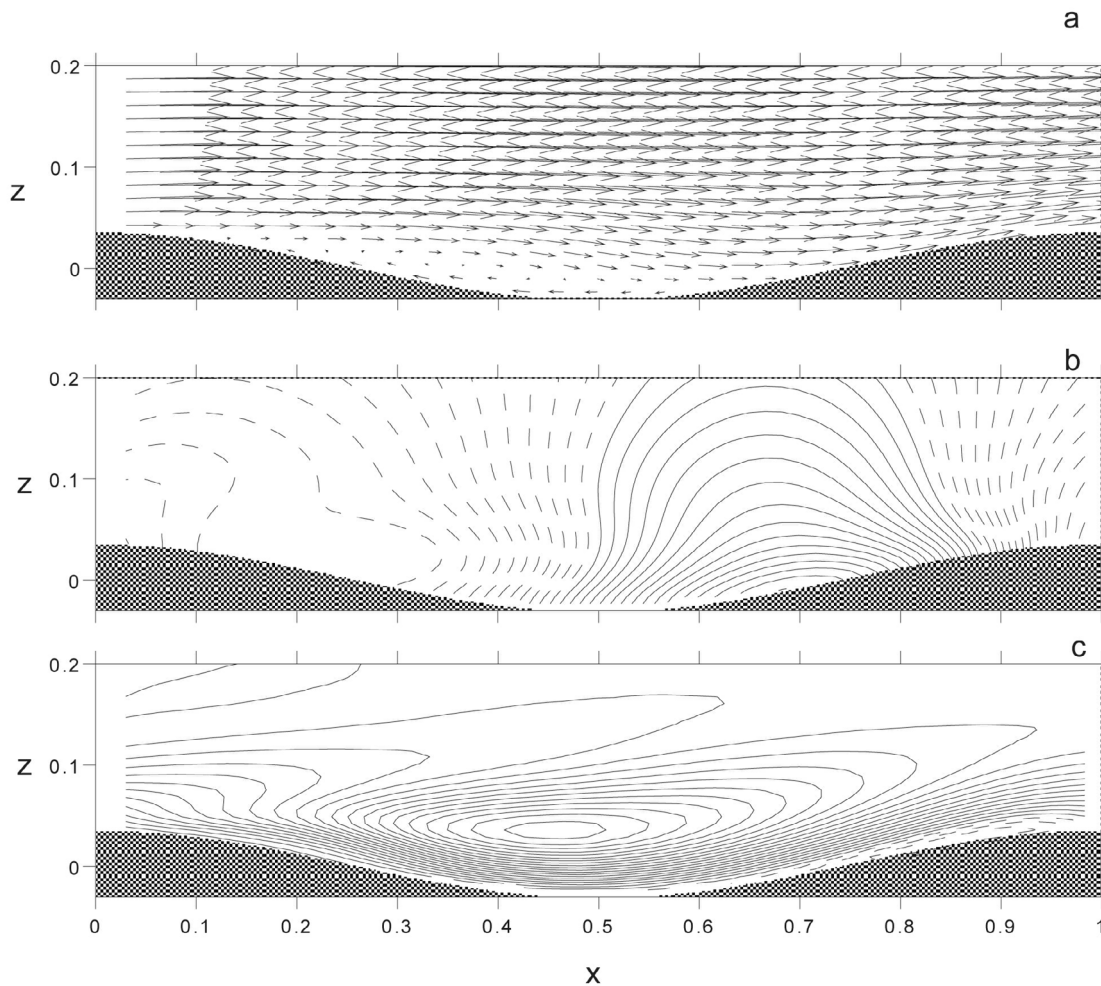 at $z = 0.042$, and (c) (y, z) plane at $x = 4.25$. (d–f) Enhanced view of the vorticity modulus field in the region $3 \leq x \leq 6, 0 \leq y \leq 2$, and $0 \leq z \leq 0.5$ in Figures 4a–4c.
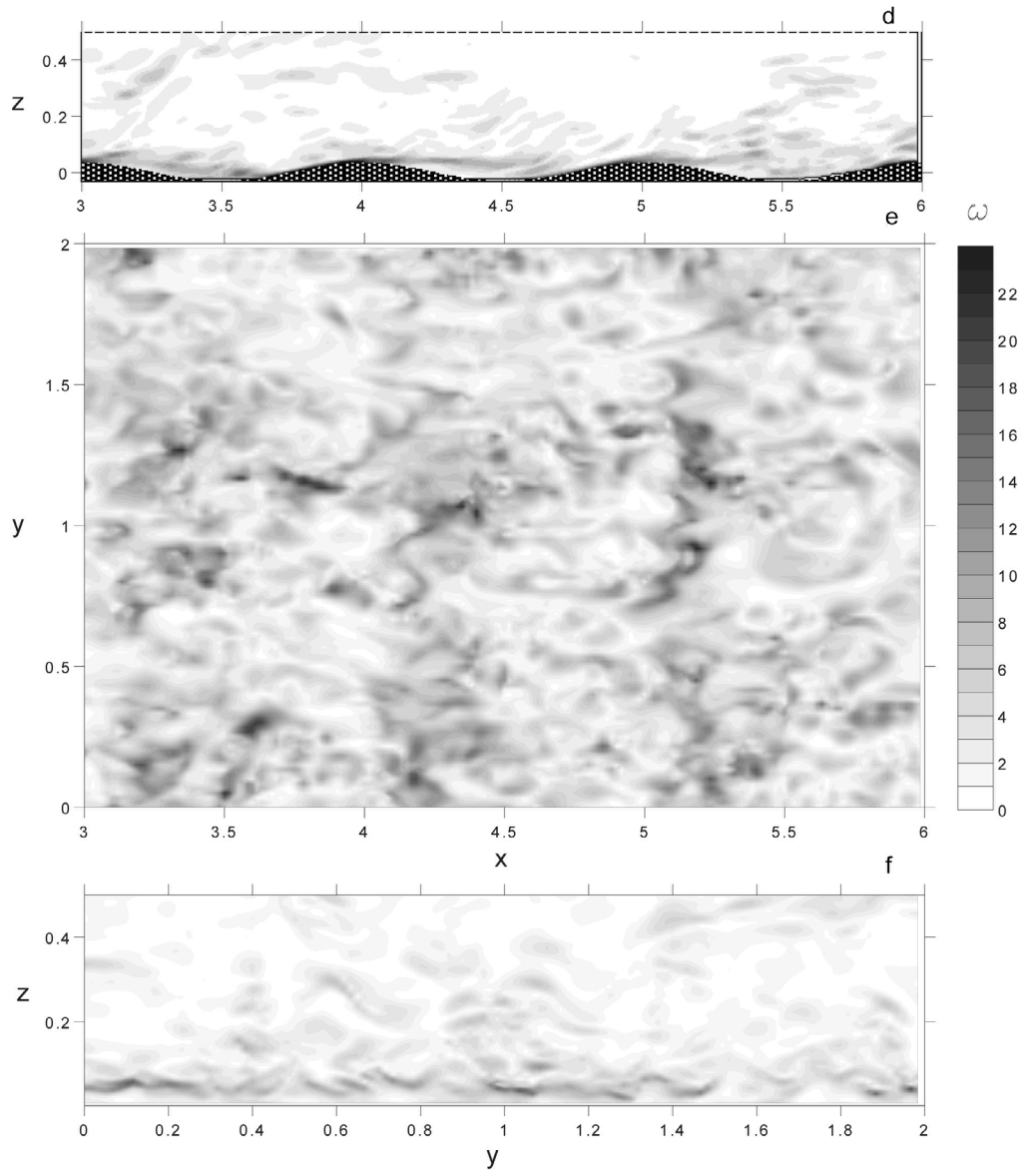
Figure 4. (continued)
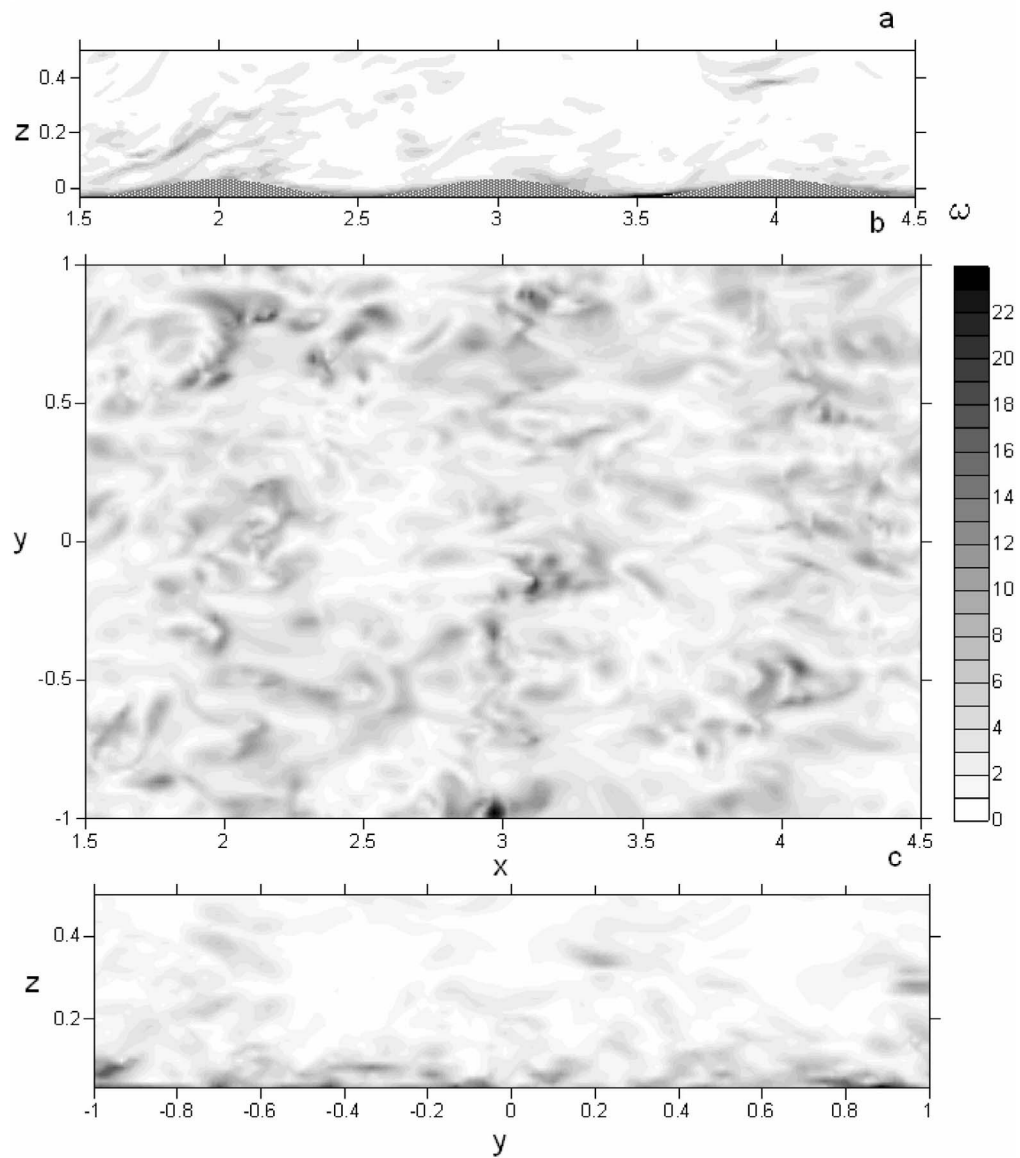
Figure 5. Instantaneous field of the vorticity modulus in the region $3 \leq x \leq 6, 0 \leq y \leq 2$, and, obtained in DNS with $ka = 0.2$ and $c = 0.2$ in the (a) (x, z) plane at $y = 0$, (b) (x, y) plane at $z = 0.042$, and (c) (y, z) plane at $x = 3$.

Figure 6.   Phase-averaged fields of (a) velocity, (b) pressure, and (c) turbulent momentum flux obtained from DNS for $c = 0.05$, $ka = 0.2$. The contours interval is 0.0005 for pressure and 0.0001 for the momentum flux. Dashed lines are for negative values.

much less present, and the vorticity is mostly concentrated in long spanwise vortex sheets lying in close vicinity of the surface, i.e., nonseparating.

[39]   Figures 6 and 7 show the distribution of the phase-averaged velocity, pressure, and turbulent momentum flux obtained in DNS for wave steepness $ka = 0.2$ and phase velocities $c = 0.05$ and 0.2, respectively. The behavior of the average fields is in general agreement with the previous numerical results of *Sullivan et al.* [2000] and *Yang and Shen* [2010]. The vector maps of the mean velocity field clearly show the Kelvin's "cat eye" pattern on the lee of the wave crest (Figures 6a and 7a). The critical layer height is smaller, and the pressure maximum is shifted windward from wave trough toward the crest for larger c (Figures 6b and 7b). Figures 6c and 7c show that a region of negative momentum flux is created on the windward side of the wave crest as the phase velocity increases.

[40]   The distribution of the mean velocity fields in Figures 5 and 6 show that the mean flow field is nonseparating, in spite of the presence of the separating thread-like vortex structures in the instantaneous flow fields (cf. Figures 4 and 5). Such a difference between the behavior of the instantaneous velocity field and the mean velocity field is caused by the inhomogeneity of the vorticity and the flow separation zones distribution along the wavefront, i.e., in the spanwise y direction.

[41]   The instantaneous flow velocity and vorticity fields averaged *only* along the wavefront (and *not* in time) are nonseparating. In order to show this, we performed y averaging of the velocity and enstrophy fields of the instantaneous flow field obtained in DNS for $ka = 0.2$ and phase velocity $c = 0.1$ ($c/u_* \approx 7$). Figure 8 compares the distributions of the instantaneous velocity and vorticity modulus fields obtained in DNS (Figures 8a–8c) and the same *instantaneous* fields after y averaging (Figures 8d and 8e). Figures 8a–8c clearly show a λ vortex separating from the wave crest at $x = 2$. Here the instantaneous flow has a separation zone. However, the y averaged vorticity and velocity
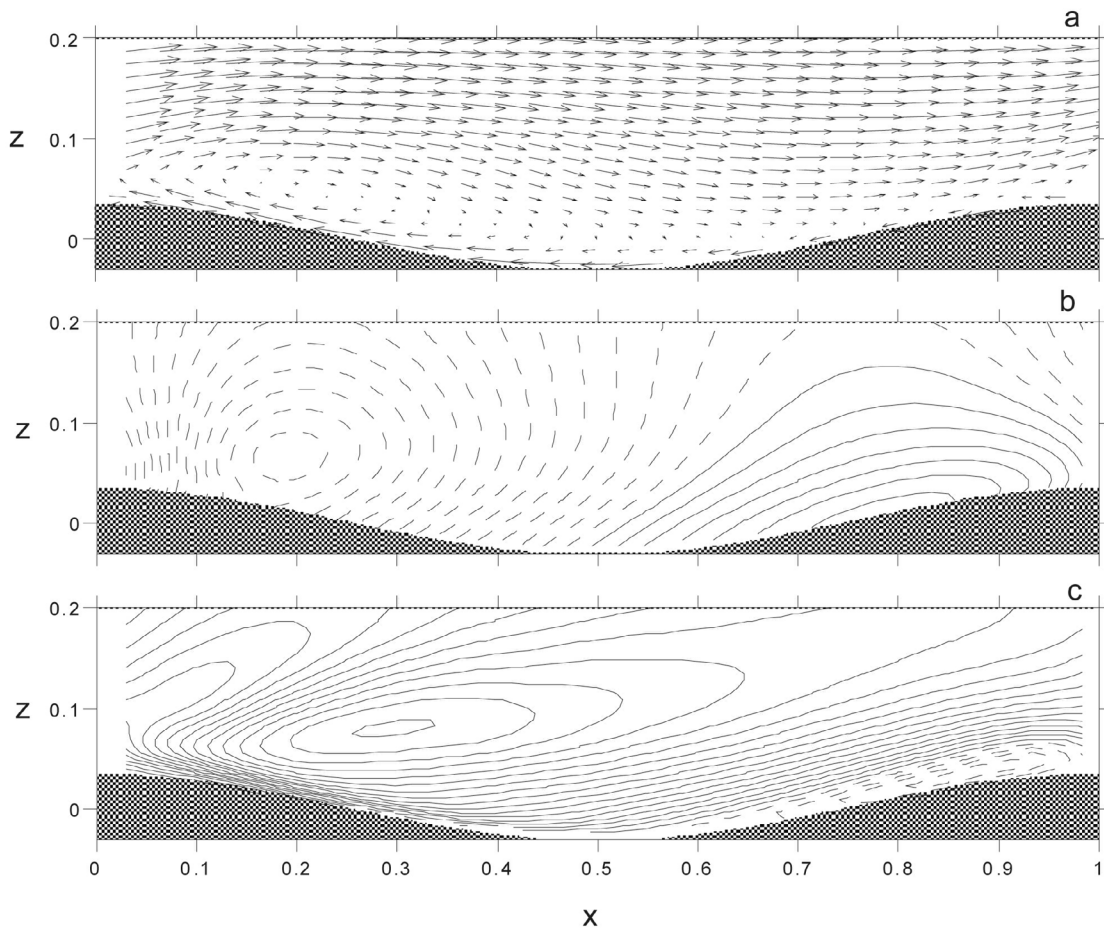
Figure 7. The same as in Figure 6 but for $c = 0.2$.

fields are smooth, nonseparating, and characterized by the well-known Kelvin's "cat eye" pattern.

[42] DNS results obtained by *Yang and Shen* [2010] also show that the instantaneous flow field has numerous separation zones whereas the ensemble-averaged field does not. Our DNS results show that the separation zones are removed after averaging of the instantaneous flow field *only* along the wavefront.

[43] The nonseparating structure of the mean flow field provides the basis for using a theoretical model developed by *Reutov and Troitskaya* [1995] for the prediction of the properties of the turbulent boundary layer over a wavy water surface. In this model, 2-D Reynolds-averaged Navier-Stokes equations are considered. The Reynolds stresses are modeled by introducing a turbulent viscosity coefficient with a given vertical profile. The RANS equations are solved analytically by the use of a quasi-linear approximation [*Jenkins*, 1992; *Reutov and Troitskaya*, 1995]. Under this approximation, only the first harmonics of the wave-induced disturbance is taken into account, and higher harmonics are neglected. The first harmonics is evaluated with the accuracy of ka, and the mean fields are evaluated with the accuracy of $(ka)^2$. Thus, in the equations for the disturbance field the terms of order $(ka)^3$ responsible for the wave-induced fields, are retained. On the other hand, the terms of

same (third-) order, responsible for interaction between the first and second harmonics, are discarded. Test calculations with the second harmonics taken into account show that this contribution is negligible for a sufficiently small wave steepness [*Jenkins*, 1992]. (A more detailed discussion of the quasi-linear model is given by *Troitskaya et al.* [2010, 2011].)

[44] Figures 9a, 9b, 10a, and 10b compare predictions of the quasi-linear model with our DNS results. Figure 9a shows vertical profiles of the mean velocity x component, $\langle U \rangle$, and the turbulent momentum flux, $-\tau = \langle u'w' \rangle$, obtained for wave steepness $ka = 0.2$ and different values of the phase velocity c. Figure 9b shows the corresponding profiles of the amplitudes and phases of the first harmonics, (u_1, w_1) and (φ_u, φ_w) of the velocity x and z components. Figures 10a and 10b present the same characteristics as in Figures 9a and 9b, but for different values of the wave steepness and phase velocity $c = 0.05$. In spite of the certain differences between the DNS results and the model prediction (e.g., for the phase φ_u with wave phase velocity $c = 0.3$ и steepness $ka = 0.2$ in Figure 9b, or for amplitudes u_1 and w_1 with wave steepness $ka = 0.2$ in Figure 10b), the agreement between the numerical and theoretical results can be regarded as satisfactory.
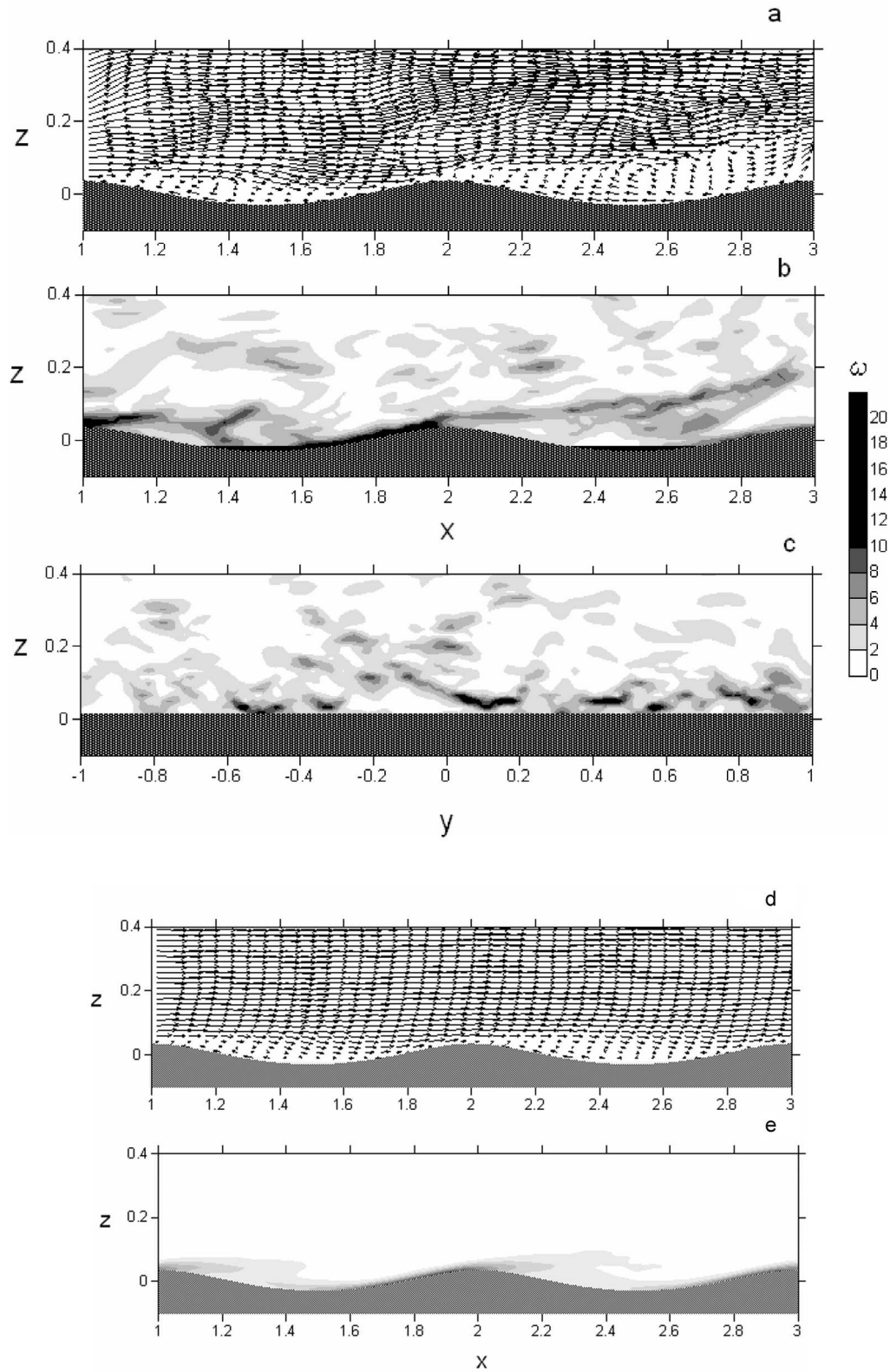
Figure 8. Instantaneous (a) velocity and (b, c) vorticity modulus fields obtained in DNS for $ka = 0.2$ and $c = 0.1$. (d, e) The same instantaneous velocity and vorticity fields as in Figures 8a–8c but averaged along the wavefront.
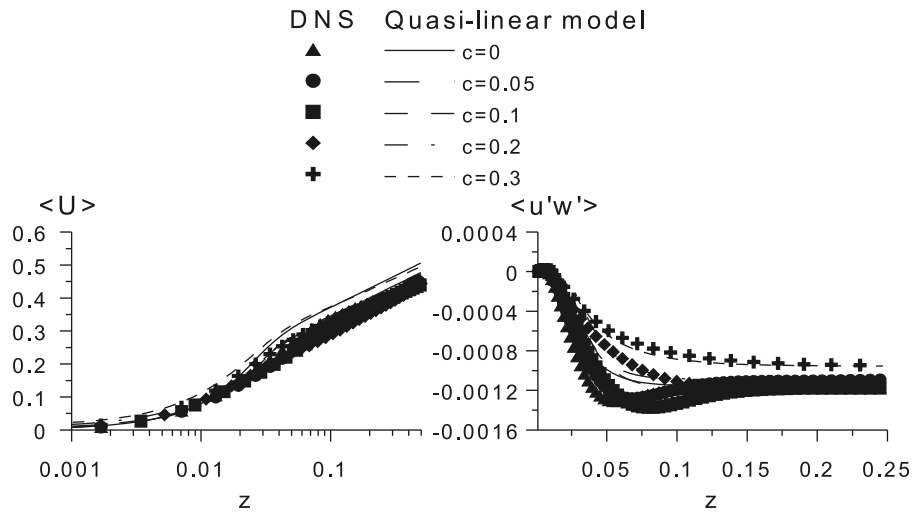
Figure 9a. Profiles of the mean horizontal velocity and turbulent momentum flux for $ka = 0.2$.
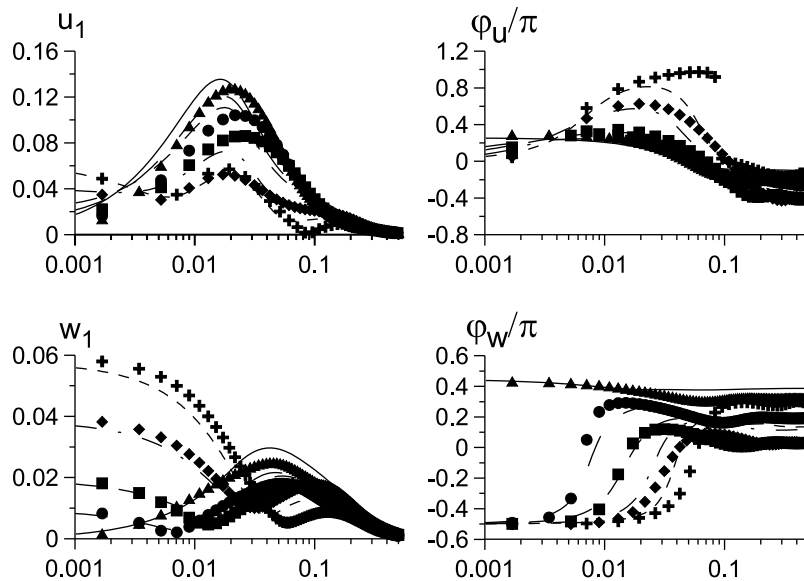

Figure 9b. Profiles of the amplitudes and phases of the first harmonics with the same notations as in Figure 9a.
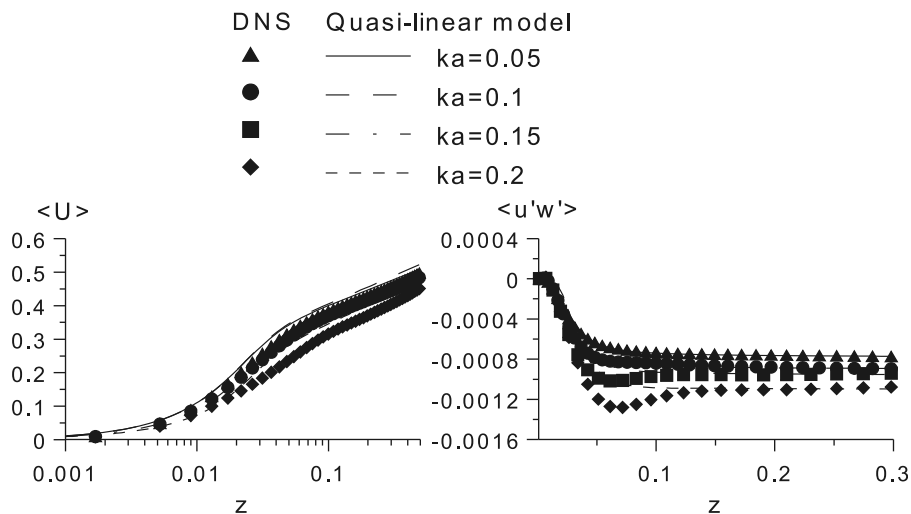
Figure 10a. Profiles of the mean horizontal velocity and turbulent momentum flux for $c = 0.05$.

[45] The quasi-linear model can be used to evaluate the first harmonics of the wave-induced pressure and wave growth rate (or form drag) which usually denoted as parameter β. This parameter is evaluated as [*Miles*, 1957]

$$\beta = \frac{2}{(ka)^2 \rho u_*^2} \frac{1}{\lambda} \int_0^\lambda \langle p \rangle \frac{dz_b}{dx} dx. \qquad (33)$$

[46] Figure 11a shows the dependence of parameter β, the pressure first harmonics amplitude and its phase on the wave age c/u^* obtained in DNS and the model prediction for $ka = 0.2$. Figure 11b shows the dependence of the same properties on ka for wave age $c/u^* = 1.7$ (phase velocity $c = 0.05$). The figure shows that the model prediction is close to the DNS

results. It is interesting to note that β in Figure 11b is a decreasing function of ka which is naturally explained by the quasi-linear model as consequence of the reduction of the turbulent momentum flux in the vicinity of the surface, where the wind-wave interaction is most efficient. Note also that the values of parameter β in Figures 11a and 11b are in good agreement with the estimate $\beta \approx 32 \pm 16$ obtained by *Plant* [1982].

5. Conclusions

[47] Direct numerical simulation of turbulent wind flow over a wavy water surface has been performed with a Reynolds number 15,000 and maximum wave steepness $ka = 0.2$. Detailed characteristics of the instantaneous and mean flow fields are obtained with high resolution of the viscous
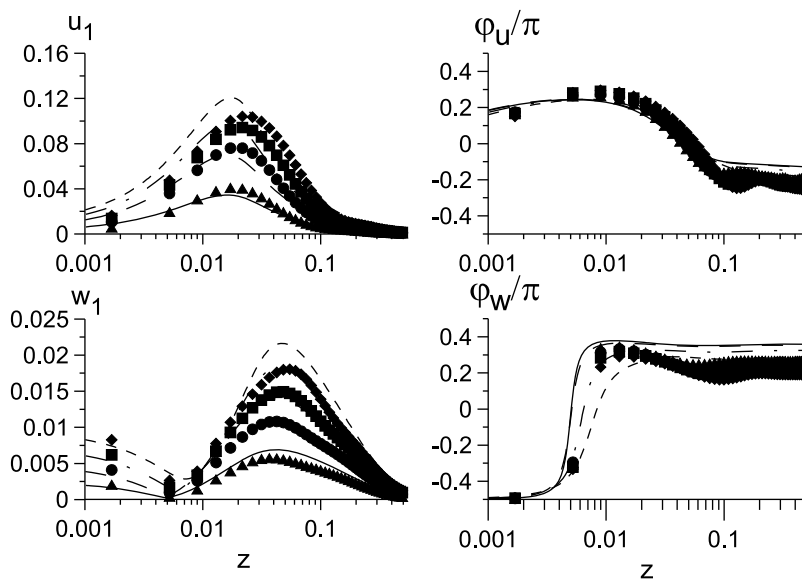

Figure 10b. Profiles of the amplitudes and phases of the first harmonics with the same notations as in Figure 10a.
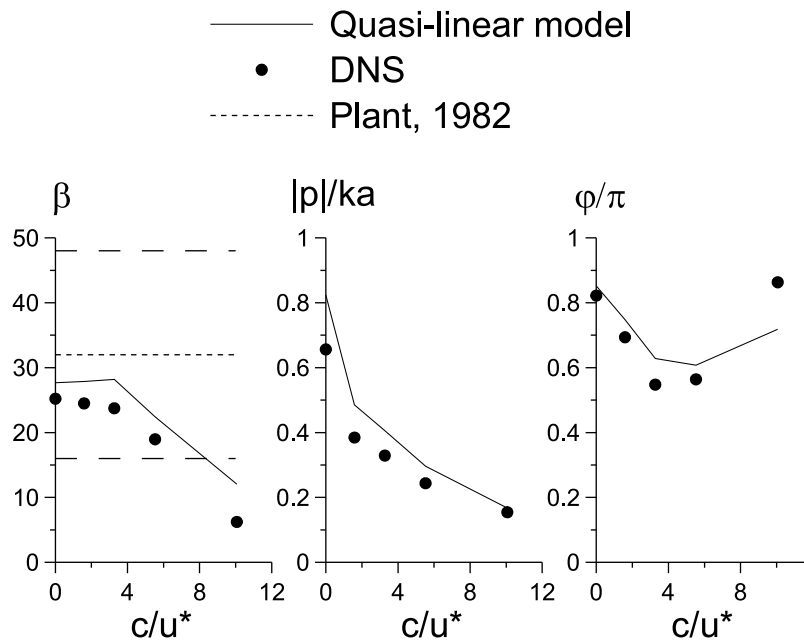
Figure 11a. Wave growth rate, first harmonics pressure amplitude, and phase versus wave age for $ka = 0.2$.

sublayer and the buffer region. The DNS results show that the instantaneous flow field is characterized by the presence of numerous separation zones in the vicinity of the wavy boundary. On the hand, the same instantaneous flow fields averaged along the wavefronts are nonseparating. The DNS are compared to the prediction of the quasi-linear model based on the RANS equations with a given profile of the turbulent viscosity coefficient. The results show that the quasi-linear model, with only the first harmonics of the wave-induced field taken into account, satisfactorily describes the properties of the mean flow field even for the cases, when flow separation is observed in the instantaneous airflow velocity fields. An explanation of applicability of the quasi-linear model is suggested due to strong inhomogenity of the separation zone in the transversal direction.

References

Adrian, R. J. (1991), Particle imaging techniques for experimental fluid dynamics, *Annu. Rev. Fluid Mech.*, *23*, 261–304, doi:10.1146/annurev.fl.23.010191.001401.

Al-Zanaidi, M. A., and W. H. Hui (1984), Turbulent airflow over water waves–a numerical study, *J. Fluid Mech.*, *148*, 225–246, doi:10.1017/S0022112084002329.

Aydin, E. M., and H. J. Leutheusser (1991), Plane-Couette flow between smooth and rough walls, *Exp. Fluids*, *11*, 302–312, doi:10.1007/BF00194862.
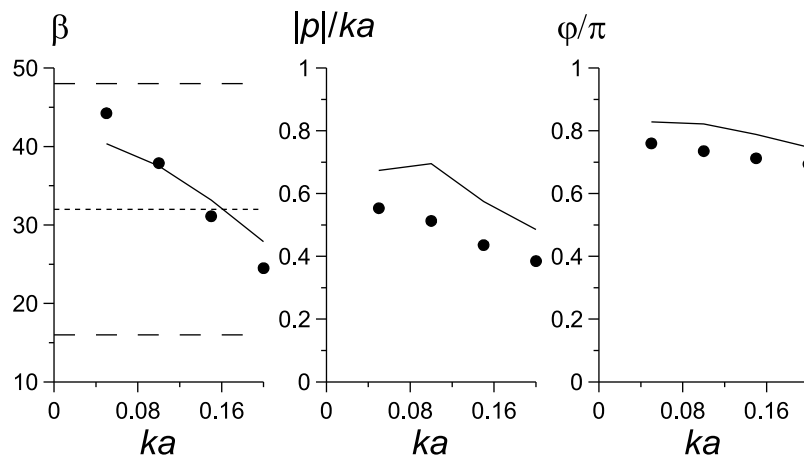
Figure 11b. Wave growth rate, first harmonics pressure amplitude, and phase versus wave steepness for $c = 0.05$ with the same notations as in Figure 11a.

Belotserkovski, O. M. (1984), *Numerical Methods in Mechanics of Continuous Media* [in Russian], Nauka, Moscow.

Chalikov, D. V. (1986), Numerical simulation of the boundary layer above water waves, *Boundary Layer Meteorol.*, *34*, 63–98, doi:10.1007/BF00120909.

Donelan, M. A., A. V. Babanin, I. R. Young, M. L. Banner, and C. McCormick (2005), Wave follower field measurements of the wind input spectral function. Part I: Measurements and calibrations, *J. Atmos. Oceanic Technol.*, *22*, 799–813, doi:10.1175/JTECH1725.1.

Fairall, C. W., E. F. Bradley, and J. E. Hare (2003), Bulk parameterization of air-sea fluxes: Updates and verification for the COARE algorithm, *J. Clim.*, *16*, 571–591, doi:10.1175/1520-0442(2003)016<0571:BPOASF>2.0.CO;2.

Fletcher, G. K. (1988), *Computational Techniques for Fluid Dynamics*, Springer, Berlin.

Gent, P. R., and P. A. Taylor (1976), A numerical model of the air flow above water waves, *J. Fluid Mech.*, *77*, 105–128, doi:10.1017/S0022112076001158.

Hsu, C. T., and E. Y. Hsu (1983), On the structure of turbulent flow over a progressive water wave: Theory and experiment in a transformed wave-following coordinate system. Part 2, *J. Fluid Mech.*, *131*, 123–153, doi:10.1017/S0022112083001263.

Hsu, C. T., E. Y. Hsu, and R. L. Street (1981), On the structure of turbulent flow over a progressive water wave: Theory and experiment in a transformed, wave-following co-ordinate system, *J. Fluid Mech.*, *105*, 87–117, doi:10.1017/S0022112081003121.

Jenkins, A. D. (1992), A quasi-linear eddy-viscosity model for the energy and momentum to wind waves using conservation-law equations in a curvilinear coordinate system, *J. Phys. Oceanogr.*, *22*, 843–858, doi:10.1175/1520-0485(1992)022<0843:AQLEVM>2.0.CO;2.

Miles, J. W. (1957), On the generation of surface waves by shear flow, *J. Fluid Mech.*, *3*, 185–204, doi:10.1017/S0022112057000567.

Moin, P., and J. Kim (1985), The structure of the vorticity field in the turbulent channel flow. Part 1. Analysis of instantaneous fields and statistical correlations, *J. Fluid Mech.*, *155*, 441–464, doi:10.1017/S0022112085001896.

Monin, A. S., and A. M. Yaglom (1971), *Statistical Fluid Mechanics*, vol. 1, MIT Press, Cambridge, Mass.

Papavassiliou, D. V., and T. J. Hanratty (1997), Transport of a passive scalar in a turbulent channel flow, *Int. J. Heat Mass Transfer*, *40*(6), 1303–1311, doi:10.1016/S0017-9310(96)00202-5.

Plant, W. J. (1982), A relationship between wind stress and wave slope, *J. Geophys. Res.*, *87*, 1961–1967, doi:10.1029/JC087iC03p01961.

Reul, N., H. Branger, and J.-P. Giovanangeli (1999), Air flow separation over unsteady breaking waves, *Phys. Fluids*, *11*, 1959–1961, doi:10.1063/1.870058.

Reutov, V. P., and Y. I. Troitskaya (1995), On the non-linear effects of the surface waves interaction with a turbulent wind [in Russian], *Izv. Acad. Sci. USSR Atmos. Oceanic Phys.*, *31*, 825–834.

Sullivan, P. P., J. C. McWilliams, and C.-H. Moeng (2000), Simulatrion of turbulent flow over idealized water waves, *J. Fluid Mech.*, *404*, 47–85, doi:10.1017/S0022112099006965.

Sullivan, P. P., J. Edson, T. Hristov, and J. C. McWilliams (2008), Large-eddy simulations and observations of atmospheric marine boundary layers above nonequilibrium surface waves, *J. Atmos. Sci.*, *65*, 1225–1245, doi:10.1175/2007JAS2427.1.

Troitskaya, Y. I., D. A. Sergeev, O. S. Ermakova, and G. N. Balandina (2010), Fine structure of the atmospheric boundary layer over the water surface [in Russian], *Izv. Acad. Sci. USSR Atmos. Oceanic Phys.*, *46*(1), 119–130.

Troitskaya, Y., D. Sergeev, O. Ermakova, and G. Balandina (2011), Statistical parameters of the air turbulent boundary layer over steep water waves measured by the PIV technique, *J. Phys. Oceanogr.*, *41*, 1421–1454, doi:10.1175/2011JPO4392.1.

Veron, F., G. Saxena, and S. K. Misra (2007), Measurements of the viscous tangential stress in the airflow above wind waves, *Geophys. Res. Lett.*, *34*, L19603, doi:10.1029/2007GL031242.

Yang, D., and L. Shen (2010), Direct-simulation-based study of turbulent flow over various waving boundaries, *J. Fluid Mech.*, *650*, 131–180, doi:10.1017/S0022112009993557.

O. A. Druzhinin and Y. I. Troitskaya, Geophysical Research, Institute of Applied Physics, Russian Academy of Sciences, Ul'yanov str. 46, Nizhni Novgorod 603950, Russia.

S. S. Zilitinkevich, Division of Atmospheric Sciences, Department of Physical Sciences, Finnish Meteorological Institute, PO Box 503, FI-00101 Helsinki, Finland.